

SPARSE MULTIDIMENSIONAL EXPONENTIAL ANALYSIS WITH AN APPLICATION TO RADAR IMAGING*

ANNIE CUYT[†], YUAN HOU[†], FERRE KNAEPKENS[†], AND WEN-SHIN LEE[‡]

Abstract. We present a d -dimensional exponential analysis algorithm that offers a range of advantages compared to other methods. The technique does not suffer the curse of dimensionality and only needs $O((d+1)n)$ samples for the analysis of an n -sparse expression. It does not require a prior estimate of the sparsity n of the d -variate exponential sum. The method can work with sub-Nyquist sampled data and offers a validation step, which is very useful in low SNR conditions. A favourable computation cost results from the fact that d independent smaller systems are solved instead of one large system incorporating all measurements simultaneously. So the method also lends itself easily to a parallel execution. Our motivation to develop the technique comes from 2D and 3D radar imaging and is therefore illustrated on such examples.

Key words. Exponential analysis, parametric method, multidimensional, sparse model, sparse data, inverse problems

AMS subject classifications. 41A21, 42A15, 42B99, 65D05 65Z05, 97M50

1. Introduction. In the past few years multidimensional exponential analysis has attracted considerable attention, as researchers were trying to solve the problem from the theoretical minimal number of samples, which equals the product of n , the number of terms in the multivariate exponential sum (2.1), and $d+1$ where d indicates the dimension (see among others [10, 30, 11]). Contrary to other approaches, the method presented in [10] does not need a full d -dimensional grid of data, nor does it require the solution of the full-size structured generalized eigenvalue problem and linear system of interpolation conditions. Instead, in [10] the linear algebra problems are split up in smaller better conditioned problems. In this paper, we develop a reliable numerical implementation, making use of this divide-and-conquer flavour and adding a sub-Nyquist sparse sampling feature to the basic theory, to deal with noisy data, tackle the numerical sensitivity in case of closely spaced exponential terms, offer output validation and provide automatically a reliable estimate of n , being the total number of terms.

Multidimensional exponential analysis is a fundamental inverse problem in signal processing, as it appears in magnetic resonance spectroscopy, MIMO radar, sonar, wireless communication, antenna array processing, sensor networks, RFID, GNSS and automotive radar, to name just a few. It is also at the basis of inverse synthetic aperture radar (ISAR) imaging, where the challenge is to extract high resolution information from noisy data, if possible using a cost effective algorithmic solution rather than an expensive advanced radar system. This application will serve as a guiding example throughout the paper.

ISAR imaging is a system that consists of a real-aperture radar, emitting a sequence of high frequency bursts, and a moving target in the far field of the radar,

*Submitted to the editors DATE.

Funding: Author Yuan Hou was financially supported by the China Scholarship Council under file no. 201706140133 and author Ferre Knaepkens was financially supported by FWO-Flanders through research project G019316N on sparse modeling.

[†]Department of Mathematics and Computer Science, University of Antwerp, Antwerp, Belgium (annie.cuyt@uantwerpen.be, yuan.hou@uantwerpen.be, ferre.knaepkens@uantwerpen.be).

[‡]Division of Computing Science and Mathematics, University of Stirling, Stirling, United Kingdom (wen-shin.lee@stir.ac.uk).

40 causing backscattering. When the target is hit by an electromagnetic wave, a limited
 41 number of locations on the object, such as edges and surface discontinuities,
 42 scatter the energy back toward the observation point. The locations of these concentrated
 43 sources of scattering energy are called scattering centers, each of which can
 44 be described by a multivariate complex exponential. ISAR is widely used and plays
 45 an important role in target identification, commercial aircraft classification, military
 46 surveillance and the like.

47 So the scattering center model in ISAR consists of a finite linear combination
 48 of complex exponentials that describe the different scattering centers of the radar
 49 target, where the number of these scattering centers is considerably less than the
 50 number of image pixels. Although the model is both simple and sparse, the inverse
 51 problem of reliably extracting the location of the scattering centers is rather sensitive
 52 to noise [37]. Therefore the problem has attracted a lot of research, which we roughly
 53 summarize below.

54 Fourier-based methods require a large densely sampled 2- or 3-dimensional data
 55 set, which may require a relatively long time to collect. Also, these techniques are
 56 trapped in the dilemma of time versus frequency resolution and cannot distinguish
 57 closely spaced scatterers, as mentioned in [20]. So several researchers have turned
 58 their attention to Prony-like spectral estimation or exponential analysis algorithms.
 59 In [27] the authors also conclude that the latter are much more accurate than Fourier
 60 based methods. But the performance of exponential analysis methods can be seriously
 61 affected by a low signal-to-noise ratio (SNR), leading to misclassifying noise as signals.

62 Here we present another Prony-like technique which allows to overcome this drawback.
 63 Also, the number of scatterers must not be estimated a priori, as pointed out in
 64 [1] for other parametric methods. In addition, the new technique does not suffer the
 65 well-known curse of dimensionality. A d -dimensional exponential analysis of an n -term
 66 model can now be carried out from a mere $O((d+1)n)$ regularly collected samples,
 67 which is substantially less than in other Prony-based methods [28, 37, 30, 16, 24, 26],
 68 where the sample usage explodes exponentially. In [37] the entailed complexity of
 69 these numerical algorithms is improved by the use of a slicing technique. The computation
 70 cost of the new method here compares much more favourably, as we solve
 71 several smaller systems instead of one large system dealing with all measurements at
 72 the same time.

73 The theory of compressive sensing also works with sparsely located data, which
 74 are however, collected randomly instead of regularly. Moreover, in radar imaging the
 75 results may be severely affected if the scattering centers on the target do not match
 76 the pre-discretized scene grid which makes up the dictionary [5]. We emphasize that
 77 methods of the Prony family do not work with a discretized grid and hence do not
 78 suffer from this drawback.

79 Other optimisation based ISAR techniques include genetic and evolutionary algorithms
 80 [19, 6]. While they are quite robust and can work completely automatic, without
 81 estimation of the model order, they require a lot of computation time, a disadvantage
 82 shared by most optimisation based methods. Several 2-dimensional compressive sensing
 83 or other optimisation approaches [34, 36, 1] may not be feasible in higher dimensions.
 84

85 The paper is organized as follows. The proposed d -dimensional exponential analysis
 86 is presented in Section 2. An additional validation of the computed results, which
 87 proves to be very useful when working with low SNR, is introduced in Section 3.
 88 The details of the exponential model governing ISAR imaging are given in Section 4,
 89 together with a first application and comparison of the new method to [16]. A way to

recondition and subsequently regularize the d -dimensional exponential analysis is explained in Section 5. The full-blown method, including validation and reconditioning, is illustrated in Section 6, where it is further compared to [30]. Among the existing d -dimensional exponential analysis generalizations, we chose to compare our 2-D and 3-D numerical illustrations to [16] and [30] for the following reasons. In Section 4.2 we compare to the 2-D Prony-like algorithm MEMP from [16] to illustrate the need for an automatic pairing of the separately computed 1-D results, as is available in the new method. In Section 6 we compare to the multidimensional ESPRIT algorithm from [30] to illustrate the importance of obtaining an automatic estimation of the sparsity n , which is considered to be a difficult problem but is solved here.

2. Multidimensional exponential analysis. The problem of d -dimensional exponential analysis consists in retrieving the linear parameters $\alpha_j \in \mathbb{C}$ and the nonlinear parameters $\phi_j \in \mathbb{C}^d$ in the exponential model

$$(2.1) \quad f(x) = \sum_{j=1}^n \alpha_j \exp(\langle \phi_j, x \rangle), \quad x = (x_1, \dots, x_d), \quad \phi_j = (\phi_{j1}, \dots, \phi_{jd})$$

from as few function samples as possible. Until recently, algorithms to solve the problem required a number of samples of the order $O(n^d)$ [16, 18, 24, 26] or $O(2^d n)$ [30] or at most $(d+1)n^2 \log^{2d-2} n$ [31], all growing exponentially with the dimension of the problem statement. In this section we present a reliable implementation which is based on [10] and requires only $O((d+1)n)$ regularly gathered samples.

Let $\Delta_1 = (\Delta_{11}, \dots, \Delta_{1d}) \neq (0, \dots, 0)$ and [22, 32]

$$(2.2) \quad |\Im(\langle \phi_j, \Delta_1 \rangle)| < \pi, \quad j = 1, \dots, n,$$

where the function $\Im(\cdot)$ returns the imaginary part of a complex number. Let us sample $f(x)$ at the points $s\Delta_1$:

$$(2.3) \quad F_s := f(s\Delta_{11}, \dots, s\Delta_{1d}), \quad s = 0, \dots, 2n-1.$$

For simplicity we also assume that the sampling direction Δ_1 is such that the values $\exp(\langle \phi_j, \Delta_1 \rangle)$, $j = 1, \dots, n$ are mutually distinct. How to deal with collisions in these values is described in [10].

The expressions $\exp(\langle \phi_j, \Delta_1 \rangle)$, $j = 1, \dots, n$ are retrieved as the generalized eigenvalues λ_j of the problem

$$(2.4) \quad \begin{pmatrix} F_1 & F_2 & \cdots & F_n \\ F_2 & \cdots & & F_{n+1} \\ \vdots & & & \vdots \\ F_n & F_{n+1} & \cdots & F_{2n-1} \end{pmatrix} v_j = \lambda_j \begin{pmatrix} F_0 & F_1 & \cdots & F_{n-1} \\ F_1 & \cdots & & F_n \\ \vdots & & & \vdots \\ F_{n-1} & F_n & \cdots & F_{2n-2} \end{pmatrix} v_j, \quad v_j \in \mathbb{C}^n$$

where the v_j denote the right eigenvectors. For the sake of completeness and for use further on, we point out that the upper left element in the left and right hand side matrices need not carry the indices 1 and 0 respectively. We can start with a higher index number instead of 0, as long as we have $2n$ consecutive samples lined up in (2.4) [7]. So the sampling of $f(x)$ in the direction of Δ_1 need not start at the origin.

In applications, the generalized eigenvalue problem (2.4) is often solved as part of a classic one-dimensional exponential analysis algorithm. In our numerical illustrations

133 we use the combination of the matrix pencil method studied in [17, 35] with the
 134 rank reduction step described in [29]. In the literature this combination is often
 135 referred to as the ESPRIT method, although the rank reduction is performed on the
 136 Hankel matrices directly instead of the covariance matrices. For the practical details
 137 concerning this aspect, the reader is referred to the Sections 4 and 6. In the Sections
 138 2, 3 and 5 the mathematical backbone of the new method is developed.

139 Because of (2.2), we can uniquely recover the inner products

$$140 \quad (2.5) \quad \Phi_j := \langle \phi_j, \Delta_1 \rangle, \quad j = 1, \dots, n$$

142 from the computed $\exp(\Phi_j)$. Although we have not yet identified the individual
 143 $\phi_{ji}, j = 1, \dots, n, i = 1, \dots, d$, nothing prevents us from already computing the linear
 144 coefficients α_j from the $2n \times n$ Vandermonde problem

$$145 \quad (2.6) \quad \begin{pmatrix} 1 & \cdots & 1 \\ \exp(\Phi_1) & \cdots & \exp(\Phi_n) \\ \vdots & & \vdots \\ \exp((2n-1)\Phi_1) & \cdots & \exp((2n-1)\Phi_n) \end{pmatrix} \begin{pmatrix} \alpha_1 \\ \vdots \\ \alpha_n \end{pmatrix} = \begin{pmatrix} F_0 \\ \vdots \\ F_{2n-1} \end{pmatrix}$$

146 Note that (2.6) reduces to a square Vandermonde system in the noise-free case, because
 147 then n of the linear equations are linearly dependent as a consequence of the fact that
 148 the values $\exp(\Phi_j)$ already satisfy (2.4).

149 In order to extract the $\phi_{ji}, j = 1, \dots, n, i = 1, \dots, d$ from the $\Phi_j, j = 1, \dots, n$,
 150 still under the assumption that the values $\exp(\Phi_j), j = 1, \dots, n$ are mutually distinct,
 151 some extra samples are required. We choose an additional $d-1$ linearly independent
 152 vectors $\Delta_2, \dots, \Delta_d$ such that the set $\{\Delta_1, \Delta_2, \dots, \Delta_d\}$ is a basis. The additional
 153 samples are then taken along a linear combination of Δ_1 and some $\Delta_i, i = 2, \dots, d$:

$$155 \quad (2.7) \quad F_{si} := f(s\Delta_1 + \Delta_i), \quad s = 0, \dots, n-1, \quad i = 2, \dots, d.$$

157 Note that only n additional samples are taken per Δ_i -shift and that they are placed
 158 equidistantly along independent shifts Δ_i with respect to the original vector Δ_1 . At
 159 the same time we assume the Nyquist constraint [22, 32]

$$160 \quad (2.8) \quad |\Im(\langle \phi_j, \Delta_i \rangle)| < \pi, \quad j = 1, \dots, n, \quad i = 2, \dots, d.$$

162 We call these vectors $\Delta_i, i = 2, \dots, d$ identification shifts because they will allow to
 163 identify the individual ϕ_{ji} in the computed Φ_j from samples taken at shifted locations.
 164 For this last step we make use of the fact that the ϕ_{ji} appear linearly in the Φ_j .

165 For i fixed, the additional samples F_{si} can be written as

$$166 \quad F_{si} = f(s\Delta_1 + \Delta_i) = \sum_{j=1}^n \alpha_j \exp(\langle \phi_j, \Delta_i \rangle) \exp(\langle \phi_j, s\Delta_1 \rangle), \quad s = 0, \dots, n-1$$

$$167 \quad = \sum_{j=1}^n A_{ji} \exp(s\Phi_j), \quad A_{ji} = \alpha_j \exp(\langle \phi_j, \Delta_i \rangle).$$

168 So for i fixed, the $A_{ji}, j = 1, \dots, n$ are obtained from the Vandermonde system

$$170 \quad (2.9) \quad \begin{pmatrix} 1 & \cdots & 1 \\ \exp(\Phi_1) & \cdots & \exp(\Phi_n) \\ \vdots & & \vdots \\ \exp((n-1)\Phi_1) & \cdots & \exp((n-1)\Phi_n) \end{pmatrix} \begin{pmatrix} A_{1i} \\ \vdots \\ A_{ni} \end{pmatrix} = \begin{pmatrix} F_{1i} \\ \vdots \\ F_{ni} \end{pmatrix}$$

171

172 of which the coefficient matrix is part of the Vandermonde structured coefficient ma-
 173 trix in (2.6). From the A_{ji} and the α_j we obtain for i fixed,

$$174 \quad (2.10) \quad \frac{A_{ji}}{\alpha_j} = \exp(\langle \phi_j, \Delta_i \rangle), \quad j = 1, \dots, n,$$

175
 176 where in the sequel we denote

$$177 \quad \Phi_{ji} := \langle \phi_j, \Delta_i \rangle, \quad j = 1, \dots, n.$$

179 Note that we have no problem to pair the Φ_{ji} to the $\Phi_j, j = 1, \dots, n$ since for each
 180 i the A_{ji} are paired to the $\alpha_j, j = 1, \dots, n$ through the Vandermonde systems (2.6)
 181 and (2.9).

182 These A_{ji} and $\exp(\Phi_{ji})$ can be computed for each $i = 2, \dots, d$. The fact that the
 183 vectors Δ_1 and $\Delta_i, i = 2, \dots, d$ are linearly independent then leads for each separate
 184 $j = 1, \dots, n$ to the $d \times d$ regular linear system

$$185 \quad (2.11) \quad \begin{pmatrix} \Delta_{11} & \cdots & \Delta_{1d} \\ \Delta_{21} & \cdots & \Delta_{2d} \\ \vdots & & \vdots \\ \Delta_{d1} & \cdots & \Delta_{dd} \end{pmatrix} \begin{pmatrix} \phi_{j1} \\ \vdots \\ \phi_{jd} \end{pmatrix} = \begin{pmatrix} \Phi_j \\ \Phi_{j2} \\ \vdots \\ \Phi_{jd} \end{pmatrix}$$

186
 187 from which the individual $\phi_{ji}, j = 1, \dots, n, i = 1, \dots, d$ are computed.

188 So all unknowns in (2.1) can be obtained at the expense of $2n$ evaluations F_s
 189 in (2.3) and $(d-1)n$ evaluations F_{si} in (2.7), or a mere total of $(d+1)n$ samples.
 190 In practice, when dealing with noisy data, the value of n is overestimated by $\eta >$
 191 n , as discussed in the next section. The minimal number of samples in an η -term
 192 exponential model of the form (2.1), in the directions Δ_1 and $\Delta_i, i = 2, \dots, d$, which
 193 is respectively 2η and η , is often again overestimated by $N \geq 2\eta$ and $\mathbf{n} \geq \eta$. The square
 194 $n \times n$ generalized eigenvalue problem (2.4), the $2n \times n$ Vandermonde system (2.6) and
 195 the $n \times n$ Vandermonde system (2.9) then respectively take the sizes $(N-\eta) \times \eta, N \times \eta$
 196 and $\mathbf{n} \times \eta$ and are all solved in the least squares sense. Sometimes some of the samples
 197 are used in a preprocessing step, such as the computation of an intermediate $(N-\eta) \times \nu$
 198 structured lower rank approximation to the Hankel matrices, where $\nu < \eta$.

199 In the next sections we describe how this technique is combined with convergence
 200 theorems from approximation theory on the one hand and sparse interpolation from
 201 computer algebra on the other hand, in order to:

- 202
- 203 • filter unstructured noise in the data out of the structured exponential model
- 204 (2.1) via a connection to Padé approximation theory,
- 205 • automatically deduce and validate the sparsity n of expression (2.1), which
- 206 is usually regarded to be a hard problem,
- 207 • separate exponential components that are contained in a cluster of similar
- 208 components, using a connection with sparse interpolation,
- 209 • and as a result of all of the above, tighten the numerical estimates for the
- 210 parameters ϕ_j and α_j in case of a low signal-to-noise ratio.
- 211

212 **3. Connection with Padé approximation: validation.** From the theoretical
 213 mathematical presentation in Section 2, we now switch to the practical situation where
 214 the samples F_s and F_{si} are contaminated by noise. For the reliable computation of

215 the parameters ϕ_j and α_j we need to add some additional steps to the algorithm. The
 216 first change is that we are going to interpret the samples as if they are coming from
 217 an η -term exponential model of the form (2.1), where $\eta > n$ is a safe overestimate of
 218 n . A connection with Padé approximation theory will then allow us to separate the
 219 noise from the actual signal content.

220 Consider the function

$$221 \quad \mathfrak{f}(z) = \sum_{s=0}^{\infty} F_s z^s.$$

222
 223 With F_s given by (2.3) we can write [33, 2]

$$224 \quad (3.1) \quad \mathfrak{f}(z) = \sum_{j=1}^n \frac{\alpha_j}{1 - \exp(\Phi_j)z}.$$

225
 226 The partial fraction decomposition (3.1) is related to the one-dimensional Laplace
 227 transform and the Z -transform of (2.1), where the inner product $\langle \phi_j, x \rangle$ is regarded
 228 as the unknown. It is a rational function of degree $n - 1$ in the numerator and degree
 229 n in the denominator with poles $1/\exp(\Phi_j)$. Now let us perturb $\mathfrak{f}(z)$ with Gaussian
 230 noise to obtain

$$231 \quad \mathfrak{f}(z) + \epsilon(z) = \sum_{s=0}^{\infty} (F_s + \epsilon_s) z^s.$$

232
 233 The theorem of Nuttall-Pommerenke states that if $\mathfrak{f}(z) + \epsilon(z)$ is analytic throughout
 234 the complex plane, except for a countable number of poles [21] and essential singu-
 235 larities [25], then its sequence of Padé approximants $\{r_{\eta-1,\eta}(z)\}_{\eta \in \mathbb{N}}$ of degree $\eta - 1$
 236 over η converges to $\mathfrak{f}(z) + \epsilon(z)$ in measure on compact sets. This means that for suf-
 237 ficiently large η , the measure of the set where the convergence is disrupted, so where
 238 $|\mathfrak{f}(z) + \epsilon(z) - r_{\eta-1,\eta}(z)| \geq \tau$ for some given threshold τ , tends to zero as η tends to
 239 infinity. Pointwise convergence is disrupted by $\eta - n$ unwanted pole-zero combinations
 240 of the Padé approximants that are added to the n true poles and $n - 1$ true zeros
 241 of $\mathfrak{f}(z)$ [13, 15], the pole and zero in the pair almost cancelling each other locally.
 242 These pole-zero combinations are referred to as Froissart doublets. In practice, these
 243 Froissart doublets offer a way to separate the noise $\epsilon(z)$ from the underlying $\mathfrak{f}(z)$
 244 [14, 15]. Because of the Padé convergence theorem, the n true (physical) poles are
 245 identified as stable poles in successive $r_{\eta-1,\eta}(z)$, while the $\eta - n$ spurious (noisy) poles
 246 are distinguished by their instability. For different η [3, 23]:

- 247
 248 • the noisy poles lie scattered in the area around the complex unit circle, and
 249 this for every different realization of the noise $\epsilon(z)$,
 250 • and the true poles $\exp(-\Phi_j)$, $j = 1, \dots, n$ are forming clusters with around
 251 each $\exp(-\Phi_j)$ cluster an almost Froissart doublet-free zone.

252
 253 This characteristic of the true poles is precisely the key point on which our method
 254 is based: after the computation of $\eta > n$ generalized eigenvalues $\lambda_j = \exp(\Phi_j)$, we
 255 discard the unstable ones and focus on the stable ones. Note that:

- 256
 257 • In order to safely rely on this convergence result, it is clear that η should be
 258 sufficiently large, as the result is more numerically accurate for η large. We
 259 usually take η to be a multiple of (the so far unknown) n .

- To decide which generalized eigenvalues are the unstable ones, the computational scheme needs to be repeated a number of times with different sets of $N + (d - 1)\mathbf{n}$ data, which can be achieved as follows.

We discuss the sampling along the Δ_1 direction first. Instead of collecting $F_s, s = 0, \dots, N - 1$ in the direction of Δ_1 , we collect some additional $F_s, s = 0, \dots, N + (\kappa - 1)\lfloor \mathbf{p}N \rfloor - 1$. Here $0 \leq \mathbf{p} \leq 1$ and $1 \leq \kappa \in \mathbb{N}$. From these samples we construct κ snapshots of N samples each, snapshot number $k = 0, \dots, \kappa - 1$ starting at $k\lfloor \mathbf{p}N \rfloor$ with an overlap of roughly $(1 - \mathbf{p})N$ points with the previous and the next snapshot. The case $\mathbf{p} = 0$ and $\kappa = 1$ delivers the single snapshot situation of the previous section.

When putting all $\kappa\eta$ generalized eigenvalues of the κ different eigenvalue problems (2.4) together, then theoretically κn of them cluster together in n clusters of each κ elements and the other $\kappa(\eta - n)$ generalized eigenvalues lie scattered around as they do not reflect true terms in the exponential model (2.1). Of course, the noise may be such that the method does not work perfectly and that in an apparent cluster somewhat less than κ elements are found. We therefore accept a cluster as soon as a sufficiently large fraction of the κ expected elements is found.

In the numerical examples we found it most useful to use a density-based cluster analysis such as DBSCAN [12]. The DBSCAN implementation requires two parameters: the density δ of the clusters and the minimum number m_δ of required cluster elements. These parameters are chosen in terms of the noise in the signal:

- Larger values of δ allow the detection of wider clusters, for instance in case of a higher noise level. Smaller values of δ lead to denser clusters with very stable estimates for the generalized eigenvalues, for instance in case of lower levels of noise.
- A value for m_δ smaller than κ allows to discard bogus estimates appearing as a consequence of outliers in the data or too high noise levels. It makes perfect sense, depending on the application, to relax m_δ to for instance $\kappa - 1, \kappa - 2$ or $\lfloor 0.9\kappa \rfloor, \lfloor 0.8\kappa \rfloor$.

A very desirable side result of the technique described in this section, is the fact that the method automatically reveals the true number n of terms in the expression (2.1) underlying all the samples: n equals the number of clusters detected by the cluster analysis.

Remains to discuss the sampling along the linearly independent shifts of Δ_1 . Here also, the data set needs to be enlarged in order to support the processing of κ snapshots. So at most we collect for each $i = 2, \dots, d$ the samples $F_{si}, s = 0, \dots, \mathbf{n} + (\kappa - 1)\lfloor \mathbf{p}N \rfloor - 1$ (for some choices of the parameters $N, \kappa, \mathbf{n}, \mathbf{p}$ not all consecutive samples are used). Remember that each of the computed $\Phi_{ji}, j = 1, \dots, \eta, i = 2, \dots, d$ is connected to its $\Phi_j, j = 1, \dots, \eta$ from the solution of the generalized eigenvalue problem (2.4). For i fixed, we therefore know which Φ_{ji} are linked to a cluster element Φ_j and which belong to a scattered Φ_j . When taking the m_δ values Φ_{ji} together that are linked to a cluster element Φ_j , then we can improve the estimate for $\Phi_{ji}, j = 1, \dots, \eta, i = 2, \dots, d$ by considering the center of gravity of the m_δ values Φ_{ji} that go together. As the Φ_{ji} are obtained from the solution of two Vandermonde structured linear systems through (2.10), their estimates are usually found to be somewhat less accurate than the estimates computed for the clustered Φ_j .

Analysis of the Φ_{ji} values when taking κ snapshots can also serve an additional purpose. Sometimes it is useful to run DBSCAN a consecutive number of times with

310 increasing values for δ . In this way, very condensed clusters are detected right from
 311 the start and more relaxed clusters are picked up in some later run. In case δ is
 312 relaxed too much, an inspection of the (at least) m_δ values Φ_{ji} associated with the
 313 (at least) m_δ estimates for a particular Φ_j in the candidate cluster, helps to accept or
 314 refute the relaxed cluster. The latter can be done by looking at the spread (standard
 315 deviation) of the associated Φ_{ji} . If this exceeds an acceptable threshold, the candidate
 316 cluster is rejected. So while a cluster of m_δ estimates for some Φ_j is “identified”, it
 317 is “confirmed” by the analysis of the m_δ associated values Φ_{ji} and this for each
 318 $i = 2 \dots, d$.

319 Let us illustrate the procedure described in the Sections 2 and 3 on some small-
 320 scale numerical examples. In Section 5 we further explain how to deal with the
 321 situation where some of the clusters around the true $\Phi_j, j = 1, \dots, n$ partially overlap,
 322 for instance because of very similar $\phi_j, j = 1, \dots, n$ in the exponential model (2.1).

323 **4. Application to ISAR imaging.** High frequency scattering toward an ob-
 324 servation point is often modeled by means of a finite number of concentrated sources
 325 of scattering energy, also called scattering centers. A radar signal backscattered from
 326 a far-field target with n scattering centers at locations $(x_j, y_j, z_j), j = 1, \dots, n$ in a
 327 cartesian coordinate system, is then decomposed into n contributions, each with a
 328 different phase and magnitude.

329 Assume the radar system emits a signal at frequency ω_h in the direction or line
 330 of sight with azimuth angle θ_g and elevation angle ϕ_m . The backscattered signal
 331 $f(h, g, m)$ with $(h, g, m) \in \mathbb{R}_+^3$ is approximated by the following sum of complex
 332 exponentials,

$$333 \quad (4.1) \quad f(h, g, m) \approx \sum_{j=1}^n \beta_j \exp\left(-\frac{4\pi i}{c}(\omega_h x_j + \omega_c \theta_g y_j + \omega_c \phi_m z_j)\right),$$

334 where β_j is the scattering amplitude of the j -th scattering center, c is the speed of
 335 light, ω_c is the central frequency $\omega_c = (\omega_0 + \omega_{(N-1)h})/2$ and the parameters ω_h, θ_g
 337 and ϕ_m are defined by

$$338 \quad \omega_h = \omega_0 + h\delta_\omega, \quad \theta_g = \theta_0 + g\delta_\theta, \quad \phi_m = \phi_0 + m\delta_\phi.$$

340 The remaining values $\omega_0, \theta_0, \phi_0$ and $\delta_\omega, \delta_\theta, \delta_\phi$ are set by the user and are system
 341 dependent. We rewrite the exponential model (4.1) as

$$342 \quad f(h, g, m) \approx \sum_{j=1}^n \alpha_j \exp\left(-\frac{4\pi i}{c}(h\delta_\omega x_j + \omega_c g\delta_\theta y_j + \omega_c m\delta_\phi z_j)\right),$$

$$343 \quad \alpha_j = \beta_j \exp\left(-\frac{4\pi i}{c}(\omega_0 x_j + \omega_c \theta_0 y_j + \omega_c \phi_0 z_j)\right).$$

344 By means of the Prony-like method presented in Section 2, the computation of the
 345 unknown scattering locations $(x_j, y_j, z_j), j = 1, \dots, n$ and the unknown scattering am-
 347 plitudes $\beta_j, j = 1, \dots, n$ is then neatly separated, with the scattering locations being
 348 delivered first after applying (2.9) and (2.10).

349 **4.1. 3-dimensional illustration of the new algorithm.** To illustrate the
 350 method on a synthetic small-scale 3-D example, we consider the 29-term exponential
 351 expression (4.1) with (x_j, y_j, z_j) and β_j given in Table 1. We further set the following

352 radar parameters:

$$\begin{aligned}
353 \quad & \omega_0 = 7.9\text{GHz}, \quad \delta_\omega = 0.0015\text{GHz}, \\
354 \quad & \theta_0 = \phi_0 = -0.024, \quad \delta_\theta = \delta_\phi = 3.75 \times 10^{-4}.
\end{aligned}$$

356 We choose (for no specific reason, except that (2.2) and (2.8) need to be satisfied): the
357 linearly independent vectors $\Delta_1 = (1.17, 0.7, 1.87)$, $\Delta_2 = (-1.00, -1.00, -1.00)$, $\Delta_3 =$
358 $(-2.10, 1.20, 3.29)$ as basis vectors for all (h, g, m) , and furthermore $N = 450$, $\nu =$
359 150 , $\eta = 100$, $\mathbf{n} = 450$, $\kappa = 10$, $\mathbf{p} = 0.1$ and start the collection of the required samples.
360 To each evaluation of (4.1) we add a Gaussian noise term of a fixed prechosen signal-
361 to-noise ratio SNR (in dB). So

$$\begin{aligned}
362 \quad & F_s = f(s\Delta_1) + \epsilon_s, \quad s = 0, \dots, M-1 := N + (\kappa-1)\lfloor \mathbf{p}N \rfloor - 1 \\
363 \quad & F_{s2} = f(s\Delta_1 + \Delta_2) + \epsilon_{M+s}, \quad s = 0, \dots, \mathbf{m}-1 := \mathbf{n} + (\kappa-1)\lfloor \mathbf{p}N \rfloor - 1 \\
364 \quad & F_{s3} = f(s\Delta_1 + \Delta_3) + \epsilon_{M+\mathbf{m}+s}, \quad s = 0, \dots, \mathbf{m}-1.
\end{aligned}$$

366 With our choices for the parameters, we sample at 855 points in the direction of Δ_1
367 and another 855 at each of the shifted locations $s\Delta_1 + \Delta_i$, $i = 2, 3$, or a total of 2565
368 points. This number is in sharp contrast with even the simplest $(\Delta_1, \Delta_2, \Delta_3)$ -grid
369 structured data set of $35 \times 35 \times 35 = 42875$ points, where we choose 35 as a very mild
370 overestimate of $n = 29$. In addition, a d -dimensional algorithm departing from a grid
371 structured data set [16] does not offer any of the advantages we have discussed so far,
372 among which:

- 373
- 374 • the natural pairing of Φ_{ji} , $i = 2, \dots, d$ to Φ_j , $j = 1, \dots, n$,
- 375 • the automatic detection of the sparsity n , and
- 376 • the validation of the computed locations (x_j, y_j, z_j) .
- 377

378 In Figure 1 we show the DBSCAN result for SNR = 10 dB with $m_\delta = \kappa - 2$ and δ varying
379 over $5^\ell \times 10^{-4}$, $\ell = 0, \dots, 4$: among the 1000 computed generalized eigenvalues ($\eta =$
380 100 , $\kappa = 10$) 29 clusters are indicated in colour. They identify the stable generalized
381 eigenvalues, which were detected and confirmed by the algorithm outlined in Section
382 2. None of the groups of m_δ associated values $\exp(\Phi_{ji})$, $j = 1, \dots, 29$, $i = 2, 3$ exhibits
383 a standard deviation larger than 0.25.

384 We also run the above example for varying noise levels, from 40 dB SNR to 5
385 dB SNR, now with $\kappa = 20$ and each experiment repeated 100 times as the noise is
386 randomly generated. In Figure 2 we show the average true cluster radius over the 29
387 scattering locations, for the generalized eigenvalues $\exp(\Phi_j)$ with $m_\delta = \kappa - 2$. This
388 true radius is computed a posteriori with the exact $\exp(\Phi_j)$ in the center. In Figure
389 3 we respectively show at the left and the right for $i = 2, 3$ the average cluster radius
390 over the 29 scattering locations, for the $\kappa - 5$ estimates closest to the true associated
391 $\exp(\Phi_{ji})$. With $\kappa = 20$, a ratio of $\kappa - 5$ over the maximum number m_δ of associated
392 elements still represents 83.3% of the associated values. In each of the Figures 2 and
393 3 we also show the smallest and largest cluster radius (dashed lines): they differ by
394 a factor of about 2. It is quite clear that the computation of the $\exp(\Phi_j)$ is more
395 accurate than that of the $\exp(\Phi_{ji})$. The estimates of the latter can be tightened but
396 this is not really important at this point.

397 **4.2. 2-dimensional illustration of the validation aspect.** In another ex-
398 periment we consider the 2-D example with 12 scattering centers (x_j, y_j) from Table
399 2. The dimension is reduced from three to two for the sole reason that in our figures

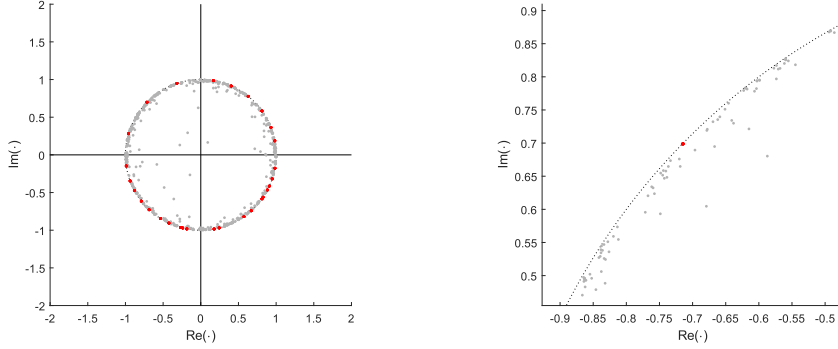


Fig. 1: The 29 clusters (red) identified by DBSCAN (left) and a zoom (right) on the stable clustered (red) versus the unstable scattered (grey) generalized eigenvalues

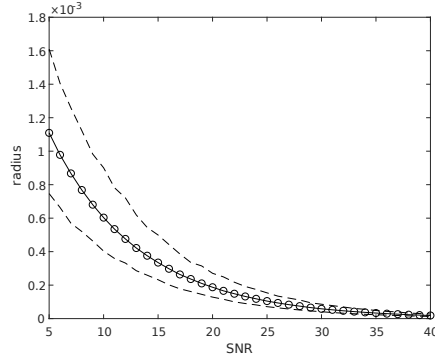


Fig. 2: Average radius of the $\exp(\Phi_j), j = 1, \dots, 29$ clusters

400 we want to use the third dimension to graph the impact of the SNR. The radar pa-
 401 rameters ω_0, θ_0 and $\delta_\omega, \delta_\theta$ are as in Section 4.1. We further take $N = 150, \nu = \eta =$
 402 $50, \mathbf{n} = 100, \kappa = 11, \mathbf{p} = 0.054$ and $\Delta_1 = (1.38, 4.14), \Delta_2 = (-7.56, 5.67)$.

In order to reduce the cluster radius in the shift direction Δ_2 we perform the shift a number of times, over $\Delta_2, 2\Delta_2, \dots, 8\Delta_2$ and combine the results, since for s fixed,

$$f(s\Delta_1 + m\Delta_2) = \sum_{j=1}^n \alpha_j \exp(\langle \phi_j, m\Delta_2 \rangle) \exp(\langle \phi_j, s\Delta_1 \rangle).$$

So the coefficients extracted from the different shifts are

$$\alpha_j \exp(\langle \phi_j, \Delta_2 \rangle), \alpha_j \exp(\langle \phi_j, 2\Delta_2 \rangle), \dots, \alpha_j \exp(\langle \phi_j, 8\Delta_2 \rangle).$$

403 The total number of collected samples then adds up to $(\kappa - 1)\lfloor \mathbf{p}N \rfloor + N$ in the Δ_1
 404 direction and $8 \times ((\kappa - 1)\lfloor \mathbf{p}N \rfloor + \mathbf{n})$ in the Δ_2 shifts, or 1670 samples altogether.

405 In Figure 4 (right) we show the result of the computations, after applying DBSCAN
 406 with $m_\delta = \kappa - 1$ and $\delta = 0.00001, 0.002505, 0.005$ to each SNR result for the Φ_j and
 407 discarding cluster results when the standard deviation of the Φ_{j2} exceeds 0.2. We let

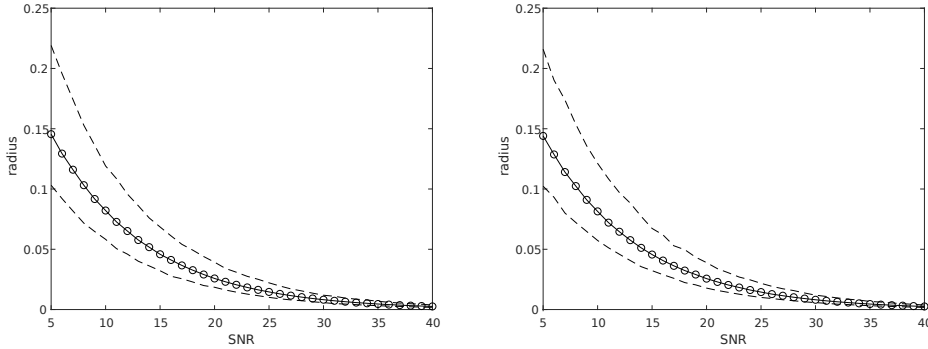


Fig. 3: Average radius of the $\exp(\Phi_{j_2}), j = 1, \dots, 29$ clusters (left) and the $\exp(\Phi_{j_3}), j = 1, \dots, 29$ clusters (right)

408 the SNR vary from 40 dB to 5 dB, top to bottom. The SNR = 10 dB slice is presented
 409 in Figure 5 (right) and a separate coordinate view is found in Figure 6 (right) where
 410 the SNR varies from right to left. For each SNR the experiment is repeated 250 times.

411 We compare these results to the output in the Figures 4 (left), 5 (left) and 6 (left)
 412 of the 2-D Prony-like algorithm MEMP [16] using the same number of samples but now
 413 laid out in a (Δ_1, Δ_2) -grid of size 40×42 . We remark the main differences with the
 414 new algorithm:

415

- 416 • the matching in the MEMP algorithm between results computed in separate
 417 dimensions is definitely not flawless, and as the noise increases erroneous
 418 combinations give rise to inexistent locations;
- 419 • the matching through the indexing of the variables in (2.6) and (2.9) leaves
 420 no room for error and so does not introduce matching errors;
- 421 • for increasing noise, meaning decreasing SNR, the unvalidated MEMP algorithm
 422 may return a few erroneous (x_j, y_j) , despite the fact that the sparsity $n = 12$
 423 was passed to the algorithm as well;
- 424 • the correct sparsity $n = 12$ need not be passed to the new algorithm, which
 425 detects it automatically as the number of identified and confirmed clusters;
- 426 • in the new algorithm the results for very small SNR are either somewhat less
 427 accurate or absent because of the high validation requirement, which can of
 428 course be relaxed by the user.

429

4.3. 3-dimensional fighter jet example. In a larger scale example of 1000
 430 scatterers depicting the surface of a fighter jet [37], we take the radar parameters
 431 as in Section 4.1, add noise with SNR = 20 dB and further choose $N = 6000, \nu =$
 432 $2000, \eta = 1500, \mathbf{n} = 6000, \kappa = 11, \mathbf{p} = 0.4$ with $\Delta_1 = (-2.2371, 0.2796, 0.8389), \Delta_2 =$
 433 $(1.6528, -1.6528, 4.9584), \Delta_3 = (0.4744, 2.1350, 0.5535)$. The density δ in DBSCAN was
 434 varied over $2^\ell \times 10^{-5}, \ell = 0, \dots, 10$ while m_δ was kept at $m_\delta = \lceil 0.8\kappa \rceil = 9$.

435

When dealing with the $\exp(\Phi_{j_i}), i = 2, 3$ we discard cluster results with a stan-
 436 dard deviation above 0.5. We remark that as the density δ increases, the probability
 437 increases that a candidate cluster, detected among the Δ_1 -projections, is not con-
 438 firmed in each and every one of the Δ_i -projections, $i = 2, \dots, d$. Rejection dominates
 439 acceptance from $\ell = 7$ on.

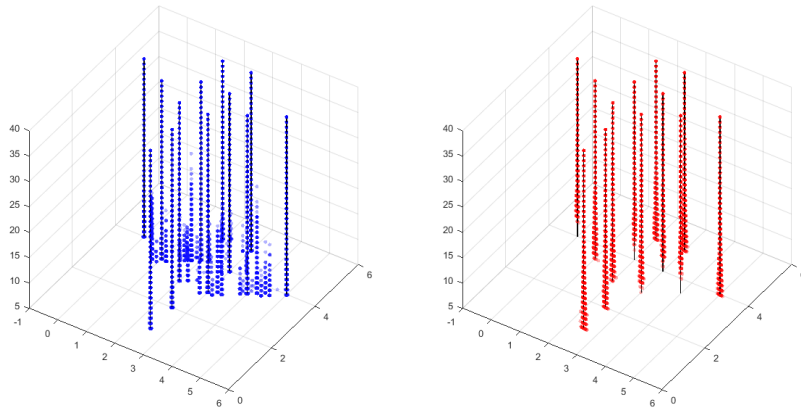


Fig. 4: Unvalidated (x_j, y_j) locations from MEMP (left) and validated (x_j, y_j) from the new algorithm (right).

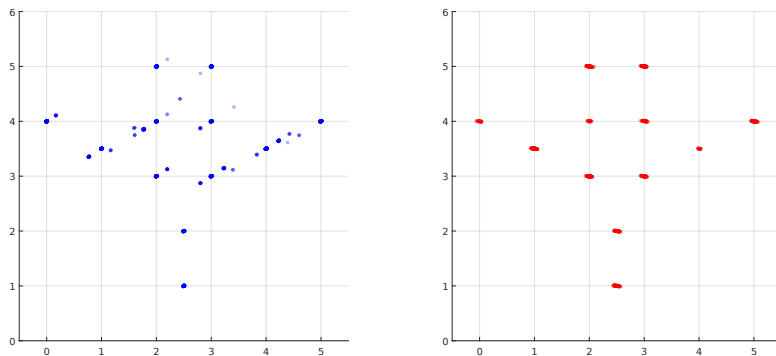


Fig. 5: Slice of Figure 4 (SNR = 10) with the colour intensity indicating the frequency of detection in the 250 runs.

440 In the end, the above algorithm detects and validates 516 scatterers (out of 1000),
 441 but misses out on the scatterers that are located too closely together or for which the
 442 inner products in (4.1) are too much alike. Although the overall shape of the fighter is
 443 correctly recognized (nose, wing tips, tail, . . .), which may be more than satisfactory
 444 for many applications, the accuracy of the algorithm can be improved in the region
 445 where several scattering centers (x_j, y_j, z_j) are located near one another, such as the
 446 windshield. To this end the algorithm needs to be combined with a sub-Nyquist
 447 technique, particularly suitable for the exponential analysis of such signals [9]. This
 448 final addition to the algorithm is explained in the next section. We also point out
 449 that, thanks to the validation step, there are no false results.

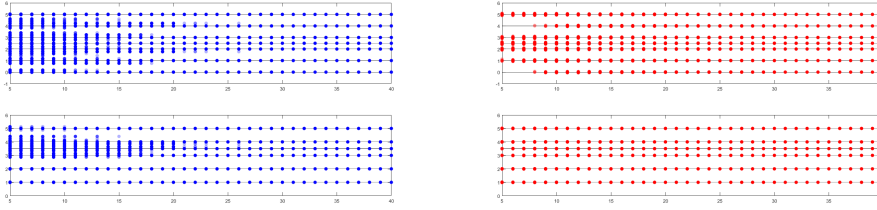


Fig. 6: Unvalidated x_j and y_j coordinates from MEMP (left) versus validated x_j and y_j coordinates from the new algorithm (right)

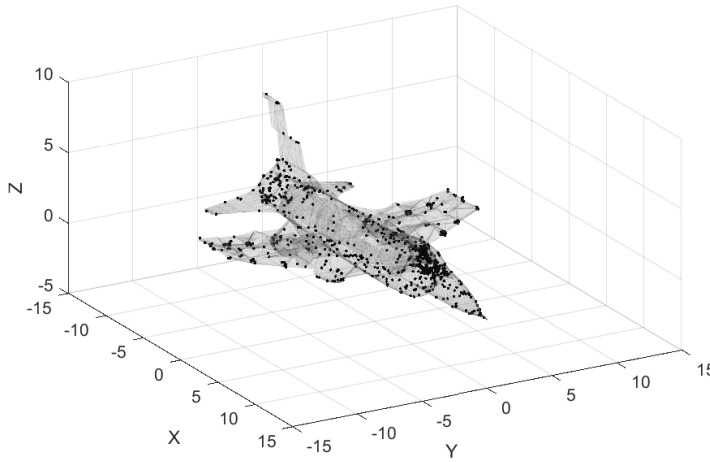


Fig. 7: Fighter jet original 1000 scattering center data

5. Connection with sparse interpolation: superresolution. We return to the notation of Section 2 to continue our presentation. When replacing the primary sampling direction Δ_1 by a multiple

$$\Delta_1(m) := m\Delta_1$$

and sampling at $s\Delta_1(m), s = 0, \dots, 2n - 1$ instead of at $s\Delta_1, s = 0, \dots, 2n - 1$, we are possibly violating the Shannon-Nyquist constraint (2.2) for $\Delta_1(m)$, when $|\Im(\langle \phi_j, \Delta_1 \rangle)| \geq \pi/m, j = 1, \dots, n$. With

$$F_s := f(s\Delta_{11}(m), \dots, s\Delta_{1d}(m)), \quad s = 0, \dots, 2n - 1,$$

the eigenvalues retrieved from (2.4) are not λ_j but [4]

$$\lambda_j(m) = \exp(m\Phi_j) = \lambda_j^m, \quad j = 1, \dots, n.$$

450 From λ_j^m the imaginary part of $\Phi_j = \langle \phi_j, \Delta_1(m) \rangle$ may not be retrieved uniquely
 451 anymore because we can only guarantee that

453 (5.1)
$$|\Im(\langle \phi_j, \Delta_1(m) \rangle)| < m\pi.$$

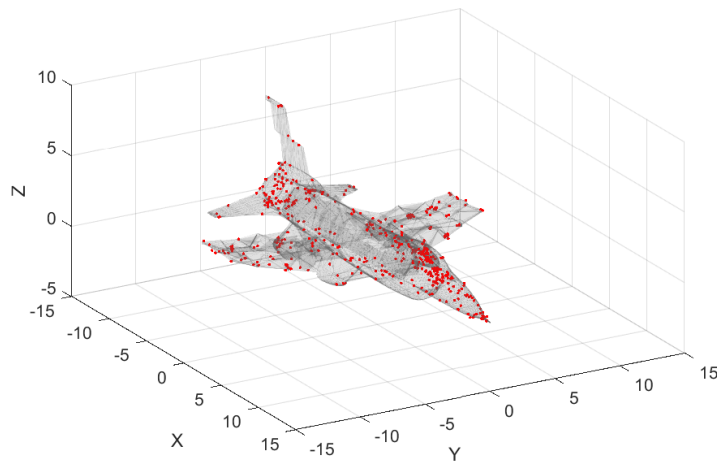


Fig. 8: Fighter jet reconstruction of 516 out of 1000 scatterers

454 So aliasing may have kicked in: because of the periodicity of $\exp(\Im(\langle \phi_j, m\Delta_1 \rangle))$ a
 455 total of m values in the $2m\pi$ wide interval (5.1) can be identified as plausible values
 456 for $\langle \phi_j, \Delta_1 \rangle$. Note that when the original λ_j are clustered, the powered λ_j^m may
 457 be distributed quite differently and unclustered. Such a relocation of the generalized
 458 eigenvalues, here referred to as superresolution, can seriously improve the conditioning
 459 of the Hankel matrices involved. In Figure 9 we show the effect of this powering on
 460 a particular example where 20 generalized eigenvalues are clustered in 5 clusters of
 461 different size.

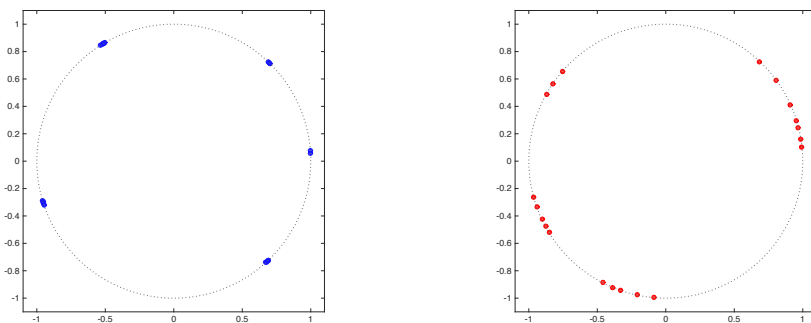


Fig. 9: Example analysis of (2.1) with $n = 20$ generalized eigenvalues: $m = 1$ (left)
 versus $m = 11$ (right)

462 What we need to resolve now is the aliasing problem that is possibly introduced
 463 by powering the generalized eigenvalues. This aliasing can be fixed at the expense
 464 of a small number of additional samples. Remember that in what follows, n
 465 everywhere be replaced by $\eta \geq n$ when using $\eta - n$ additional terms to model the

466 noise.

To fix the aliasing, we add n samples to the collection $F_0, F_m, \dots, F_{(2n-1)m}$, namely at the shifted points

$$s\Delta_1(m) + \mu\Delta_1 = (sm + \mu)\Delta_1, \quad s = r, \dots, r + n - 1, \quad 0 \leq r \leq n.$$

467 An easy choice for μ is a (small) number mutually prime with m (for the most gen-
468 eral choice allowed, we refer to [8]). With the additional samples we proceed as follows:

469

- 470 • From the samples $F_0, F_m, \dots, F_{(2n-1)m}$ we first compute the generalized ei-
471 genvalues λ_j^m and the coefficients α_j going with λ_j^m in the model

$$472 \quad (5.2) \quad F_{sm} = f(sm\Delta_1) = \sum_{j=1}^n \alpha_j \exp(\langle \phi_j, sm\Delta_1 \rangle)$$

$$473 \quad (5.3) \quad = \sum_{j=1}^n \alpha_j \lambda_j^{sm}, \quad s = 0, \dots, 2n - 1.$$

474

475 We know which coefficient α_j goes with which generalized eigenvalue λ_j^m , but
476 we just cannot identify the correct $\mathfrak{S}(\langle \phi_j, \Delta_1 \rangle)$ from λ_j^m .

- 477 • Next we deal with the samples at the additional locations $sm\Delta_1 + \mu\Delta_1$, which
478 satisfy

$$479 \quad (5.4) \quad F_{sm+\mu} = f(sm\Delta_1 + \mu\Delta_1) = \sum_{j=1}^n \alpha_j \exp(\langle \phi_j, (sm + \mu)\Delta_1 \rangle)$$

$$480 \quad (5.5) \quad = \sum_{j=1}^n (\alpha_j \lambda_j^\mu) \lambda_j^{sm}, \quad s = r, \dots, r + n - 1.$$

481

482 This system is a linear system with a similar Vandermonde structured co-
483 efficient matrix as in (5.2), but now with a new left hand side $F_{sm+\mu}$ and
484 unknown coefficients $\alpha_1 \lambda_1^\mu, \dots, \alpha_n \lambda_n^\mu$ instead of $\alpha_1, \dots, \alpha_n$. And again we
485 can associate each computed $\alpha_j \lambda_j^\mu$ with the proper generalized eigenvalue
486 λ_j^m , because of the indexing of the variables and coefficients.

- 487 • Then, by dividing the $\alpha_j \lambda_j^\mu$ computed from (5.4) by the α_j computed from
488 (5.2), for $j = 1, \dots, n$, we obtain from each quotient λ_j^μ a second set of μ
489 plausible values for $\langle \phi_j, \Delta_1 \rangle$ in the $2\mu\pi$ wide interval $|\mathfrak{S}(\langle \phi_j, \mu\Delta_1 \rangle)| < \mu\pi$.
- 490 • Because of the fact that we choose μ and m relatively prime, the two sets
491 of plausible values for $\langle \phi_j, \Delta_1 \rangle$ have only one value in their intersection [9].
492 Thus the aliasing problem is solved: each $\langle \phi_j, \Delta_1 \rangle$ is retrieved uniquely from
493 the computation of both λ_j^m and λ_j^μ for $j = 1, \dots, n$.

494

495 This multidimensional sub-Nyquist sampling strategy may help us determine the
496 clustered scattering centers occurring in Section 4.3. As suggested in Figure 9, the
497 technique spreads out the generalized eigenvalues, which may recondition the inverse
498 problem. In addition, a variation of scale factors m may be used and the idea can be
499 translated to the sampling at the shifted locations involving the identification shifts
500 $\Delta_2, \dots, \Delta_d$ which satisfy (2.8).

501 To illustrate how the combined algorithm, laid out in the Sections 2, 3 and 5 works,
502 we take up the challenging example of Section 4.3 again to return highly accurate

503 results on about 95% of the scattering locations. The result is also compared to
 504 another d -dimensional generalization, called ND-ESPRIT, which arranges the samples
 505 in multilevel Hankel matrices [30].

506 **6. Full scale ISAR illustration.** When returning to the example in Section
 507 4.3, we take the radar parameters, the signal-to-noise ratio and the vectors $\Delta_i, i =$
 508 $1, 2, 3$ as specified there. We collect 30000 samples $F_s = f(s\Delta_1)$ and 30000 samples
 509 $F_{si} = f(s\Delta_1 + \Delta_i), i = 2, 3$ along each of the shifts, so a total of 90000 samples in total.
 510 These samples are now reorganized as follows for use with the technique described in
 511 Section 5.

512 With the total of 90000 samples we perform the following analyses. For each of
 513 the analyses we take $N = 6000, \nu = 2000, \eta = 1500, \mathbf{n} = 6000$. The remaining param-
 514 eters for the sub-Nyquist sampling in the direction Δ_1 are:

515

- 516 • $m = 2, \mu = 1, \kappa = 6, \mathbf{p} = 0.3;$
- 517 • $m = 3, \mu = 1, \kappa = 4, \mathbf{p} = 2/9;$
- 518 • $m = 4, \mu = 1, \kappa = 3, \mathbf{p} = 0.125.$

519

520 In each of the above analyses, the sampling in the direction Δ_1 starts with F_0
 521 and continues with F_m, F_{2m}, \dots . The shifted samples, that serve the purpose of re-
 522 pairing the possible sub-Nyquist aliasing effect, start with F_1 and continue with
 523 F_{m+1}, F_{2m+1}, \dots . In order to make good use of the samples inbetween, the proce-
 524 dure can be repeated $m - 1$ times with the same m and μ but now starting the
 525 sampling, instead of at F_0 , at F_1 and then at F_2 and so on till F_{m-1} . In this way a
 526 choice of m produces $m\kappa$ estimates for the $\exp(\Phi_i), i = 1, \dots, \eta$ instead of κ , and thus
 527 provides a sound basis for validation since $m\kappa$ is usually sufficiently large.

528 For the choices above, we have $m\kappa = 12$ for $m = 2, 3, 4$ and so we can take, for
 529 instance, $m_\delta = (5/6)m\kappa = 10$. In Figure 10 (left and right), we show how accurate the
 530 scattering centers are reconstructed, under SNR = 20 dB noise: with every scattering
 531 center in the original data we associate the \log_{10} of the Euclidean distance to the
 532 nearest reconstructed scattering center (in meter on the x -axis) and then accumulate
 533 these (tally is on the y -axis). The distinction between the two figures is that Figure
 534 10 (left) is the result for $m = 1$ (516 scatterers reliably identified), without the use
 535 of the enhancement given in Section 5, and Figure 10 (right) is the result for $m = 4$
 536 (696 scatterers detected and validated).

537

538 The improvement from $m = 1$ to $m = 4$ may not seem very impressive at first
 539 sight. But note that the accurately reconstructed scattering centers (say $\log_{10}(\cdot) \leq$
 540 -1) from $m = 1$, need not be the same as the accurately reconstructed ones from
 541 the use of $m = 4$. Therefore the combination of both results, merely joining the
 542 reconstructions from $m = 1$ with the 696 reconstructions from $m = 4$, immediately
 543 leads to the improved distance graph shown in Figure 11.

543

544 Eventually, all runs executed with $m = 1, 2, 3, 4$ can be combined, merely joining
 545 all the computed scatterer reconstructions: 516 from $m = 1$, 667 from $m = 2$, 673 from
 546 $m = 3$ and 696 from $m = 4$, adding up to 2552 in total, with many of them (almost)
 547 duplicates. This then leads to highly accurate results for most of the scatterers. In
 548 Figure 12 we see that in this combined output 81% of the scatterers is reconstructed
 549 within an error of at most 10 cm and 95% is found within a distance of 30 cm! Only
 550 3 scatterers are not reconstructed within a distance of 1 m. The most inaccurately
 551 reconstructed scatterer in Figure 13 is near the engine outlet, where one can note that
 one reconstruction is slightly off. In Figure 13 the 2552 reconstructions are displayed

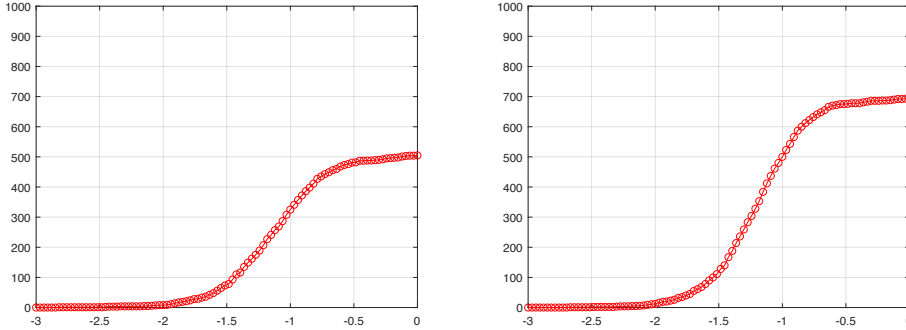


Fig. 10: Accuracy of the reconstructed scatterers for $m = 1$ (left) and $m = 4$ (right) versus the data (\log_{10} of the Euclidean distance)

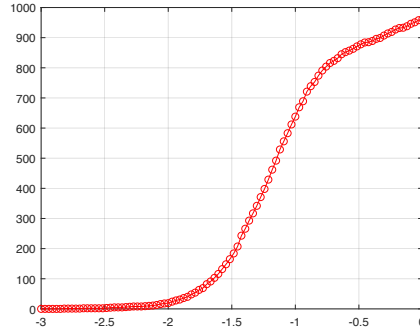


Fig. 11: Accuracy of the reconstructed scatterers ($m = 1$ and $m = 4$ combined) versus the data (\log_{10} of the Euclidean distance)

552 altogether. Note that, thanks to the validation technique, there are no false results, as
 553 also pointed out for Figure 8 where the sub-Nyquist subdivision of the data samples
 554 is not yet put to work.

555 Remains to compare the result to that of a d -dimensional Prony-type algorithm,
 556 such as [30] from data laid out in a grid. For instance, a $45 \times 45 \times 45$ grid consists of
 557 91125 samples, which compares nicely to the 90000 samples used in our method. The
 558 d -dimensional version considered in [30] starts with the construction of a multilevel
 559 Hankel matrix, for which we take 26×20 Hankel blocks on all $d = 3$ levels, thus
 560 totalling up to a $26^3 \times 20^3$ or 17576×8000 matrix. A log-plot of its singular values is
 561 shown in Figure 14 (left), from which one can deduce that $n \approx 467$ (point of maximal
 562 curvature of the plot). With 20 dB noise added to the data, the Euclidean distance
 563 log-plot for the 467 reconstructed scatterers is as in Figure 14 (right). This graph
 564 somewhat compares to the graphs in Figure 10 but is far from the result displayed in
 565 Figure 12 which can be attained with the same sample usage. In Figure 15 we show
 566 the actual 467 reconstructed scatterers superimposed on the fighter jet.

567 One may wonder what the role is, played by the total number of 90000 collected

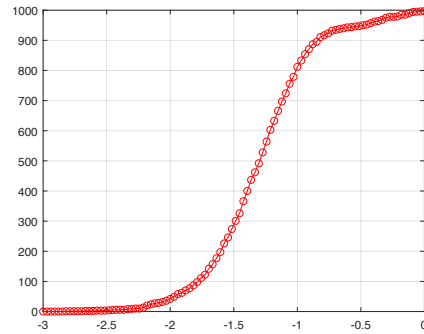


Fig. 12: Accuracy of the reconstructed scatterers ($m = 1, 2, 3, 4$ combined) versus the data (\log_{10} of the Euclidean distance)

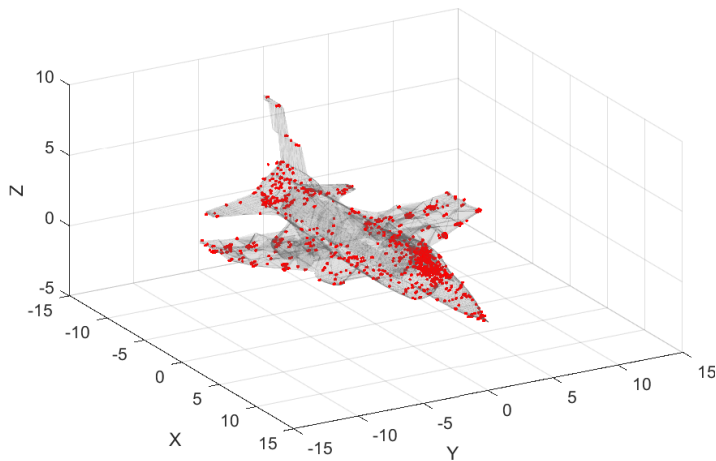


Fig. 13: Fighter jet reconstruction of 934 out of 1000 scatterers

568 samples for our method, in the Figures 10 to 13. When reducing the sampling from
 569 30000 along each of the 3 directions to 24000, then 71% of the scatterers is found
 570 within a distance of 10 cm and 93% within 30 cm. When increasing the sampling
 571 from three times 30000 to three times 60000, then as expected, the reconstruction
 572 improves, namely 94% is found within 10 cm and 98% within 30 cm.

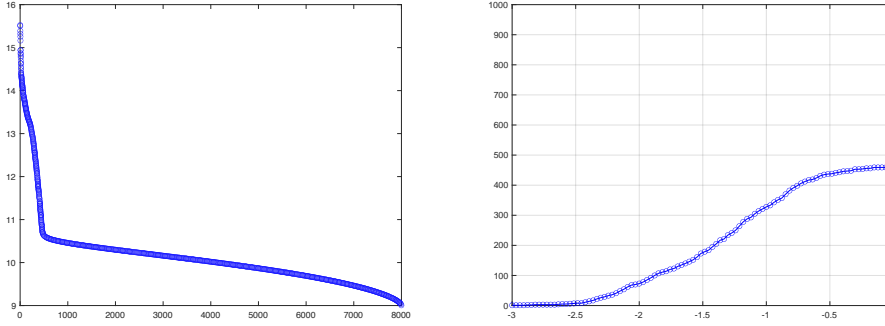


Fig. 14: Singular values of the multilevel Hankel matrix (left log-plot) and distance error of the reconstructed scatterers (right log-plot) using [30]

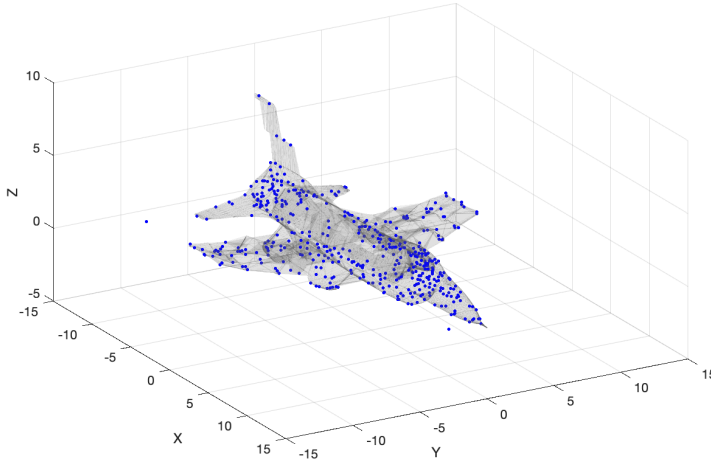


Fig. 15: Fighter jet reconstruction of 467 scatterers using the method in [30]

j	x_j	y_j	z_j	β_j	j	x_j	y_j	z_j	β_j
1	-9.25	0.77	-9.10	53.40	16	-0.59	-8.07	2.44	38.80
2	-8.51	0.77	-7.34	52.50	17	1.93	9.00	4.18	37.6
3	-7.75	0.77	-5.65	51.30	18	1.93	7.22	4.18	36.90
4	-5.15	2.99	-3.19	50.60	19	1.93	-8.07	4.18	35.70
5	-5.15	-2.55	-3.19	49.30	20	1.93	-6.22	4.18	34.90
6	-4.31	4.33	-1.85	48.20	21	2.99	0.77	4.18	33.80
7	-4.31	-4.11	-1.85	47.50	22	4.46	0.77	5.50	32.60
8	-2.61	7.22	0.59	46.30	23	5.87	2.99	6.55	31.50
9	-2.61	-6.22	0.59	45.70	24	5.87	-2.55	6.55	30.80
10	-0.59	9.00	2.44	44.40	25	7.02	2.99	7.52	29.90
11	-0.59	4.33	2.44	43.20	26	7.02	-2.55	7.52	28.70
12	-0.59	2.99	2.44	42.00	27	8.67	2.99	8.42	27.60
13	-0.59	-0.80	2.44	41.20	28	8.67	0.77	8.42	26.50
14	-0.59	-2.55	2.44	40.50	29	8.67	-2.55	8.42	25.10
15	-0.59	-4.11	2.44	39.60					

Table 1: 29-term 3-dimensional ISAR problem.

j	x_j	y_j	β_j
1	0.00	4.00	50.00
2	1.00	3.50	50.00
3	2.00	5.00	50.00
4	2.00	4.00	50.00
5	2.00	3.00	50.00
6	2.50	2.00	50.00
7	2.50	1.00	50.00
8	3.00	5.00	50.00
9	3.00	4.00	50.00
10	3.00	3.00	50.00
11	4.00	3.50	50.00
12	5.00	4.00	50.00

Table 2: 12-term 2-dimensional ISAR problem.

573 **Acknowledgments.** The authors are indebted to the colleagues from [37] for
 574 emailing them the scattering center data of the fighter jet used in the examples.

575

REFERENCES

- 576 [1] A. BACCI, E. GIUSTI, D. CATALDO, S. TOMEI, AND M. MARTORELLA, *ISAR resolution enhance-*
 577 *ment via compressive sensing: A comparison with state of the art SR techniques*, in 2016
 578 4th International Workshop on Compressed Sensing Theory and its Applications to Radar,
 579 Sonar and Remote Sensing (CoSeRa), IEEE, 2016, pp. 227–231.
- 580 [2] Z. BAJZER, A. C. MYERS, S. S. SEDAROUS, AND F. G. PRENDERGAST, *Padé-Laplace method*
 581 *for analysis of fluorescence intensity decay*, Biophys. J., 56 (1989), pp. 79–93.
- 582 [3] P. BARONE, *On the distribution of poles of Padé approximants to the Z-transform of complex*
 583 *Gaussian white noise*, Journal of Approximation Theory, 132 (2005), pp. 224–240, <https://doi.org/10.1016/j.jat.2004.10.014>.
- 584 [4] M. BRIANI, A. CUYT, AND W. LEE, *Validated exponential analysis for harmonic sounds*, in
 585 DAFX17, 20th international conference on digital audio effects, vol. 20, Edinburgh, United
 586 Kingdom, 2017, pp. 222–227.
- 587 [5] Y. CHI, L. L. SCHARF, A. PEZESHKI, AND A. R. CALDERBANK, *Sensitivity to basis mismatch*
 588 *in compressed sensing*, IEEE Transactions on Signal Processing, 59 (2011), pp. 2182–2195.
- 589 [6] L.-S. CHOI AND H.-T. KIM, *One-dimensional evolutionary programming-based CLEAN*, Elec-
 590 tronics Letters, 37 (2001), pp. 400–401.
- 591 [7] A. CUYT AND W.-S. LEE, *Sparse interpolation and rational approximation*, vol. 661 of Contem-
 592 porary Mathematics, Providence, RI, 2016, American Mathematical Society, pp. 229–242,
 593 <https://doi.org/10.1090/conm/661/13284>.
- 594 [8] A. CUYT AND W.-S. LEE, *An analog Chinese Remainder Theorem*, tech. report, Universiteit
 595 Antwerpen, 2017.
- 596 [9] A. CUYT AND W.-S. LEE, *How to get high resolution results from sparse and coarsely sampled*
 597 *data*, Appl. Comput. Harmon. Anal., (2018), <https://doi.org/10.1016/j.acha.2018.10.001>.
 598 To appear.
- 599 [10] A. CUYT AND W.-S. LEE, *Multivariate exponential analysis from the minimal number*
 600 *of samples*, Adv. Comput. Math., 44 (2018), pp. 987–1002, [https://doi.org/10.1007/](https://doi.org/10.1007/s10444-017-9570-8)
 601 [s10444-017-9570-8](https://doi.org/10.1007/s10444-017-9570-8).
- 602 [11] B. DIEDERICHS AND A. ISKE, *Parameter estimation for bivariate exponential sums*, in IEEE In-
 603 ternational Conference Sampling Theory and Applications (SampTA2015), 2015, pp. 493–
 604 497, <https://doi.org/10.1109/SAMP.TA.2015.7148940>.
- 605 [12] M. ESTER, H.-P. KRIEGEL, J. SANDER, AND X. XU, *A density-based algorithm for discovering*
 606 *clusters in large spatial databases with noise*, in KDD’96 Proceedings of the Second In-
 607 ternational Conference on Knowledge Discovery and Data Mining, KDD-96, AAAI Press,
 608 1996, pp. 226–231.
- 609 [13] J. GAMMEL, *Effect of random errors (noise) in the terms of a power series on the convergence*
 610

- 611 *of the Padé approximants*, in Padé approximants, P. Graves-Morris, ed., 1972, pp. 132–133.
- 612 [14] J. GILEWICZ AND M. PINDOR, *Padé approximants and noise: a case of geometric series*, J.
- 613 Comput. Appl. Math., 87 (1997), pp. 199–214, [https://doi.org/10.1016/S0377-0427\(97\)](https://doi.org/10.1016/S0377-0427(97)00185-4)
- 614 [00185-4](https://doi.org/10.1016/S0377-0427(97)00185-4).
- 615 [15] J. GILEWICZ AND M. PINDOR, *Padé approximants and noise: rational functions*, J. Comput.
- 616 Appl. Math., 105 (1999), pp. 285–297, [https://doi.org/10.1016/S0377-0427\(99\)00041-2](https://doi.org/10.1016/S0377-0427(99)00041-2).
- 617 [16] Y. HUA, *Estimating Two-dimensional Frequencies by Matrix Enhancement and Matrix Pencil*,
- 618 IEEE Transactions on Signal Processing, 40 (1992), pp. 2267–2280.
- 619 [17] Y. HUA AND T. K. SARKAR, *Matrix pencil method for estimating parameters of exponentially*
- 620 *damped/undamped sinusoids in noise*, IEEE Trans. Acoust. Speech Signal Process., 38
- 621 (1990), pp. 814–824, <https://doi.org/10.1109/29.56027>.
- 622 [18] S. KUNIS, T. PETER, T. RÖMER, AND U. VON DER OHE, *A multivariate generalization of Prony's*
- 623 *method*, Linear Algebra and its Applications, 490 (2016), pp. 31–47.
- 624 [19] Q. LI, E. J. ROTHWELL, K.-M. CHEN, AND D. P. NYQUIST, *Scattering center analysis of radar*
- 625 *targets using fitting scheme and genetic algorithm*, IEEE Transactions on Antennas and
- 626 Propagation, 44 (1996), pp. 198–207.
- 627 [20] Q. LIU, A. LIU, Y. WANG, AND H. LI, *A super-resolution sparse aperture ISAR sensors imag-*
- 628 *ing algorithm via the MUSIC technique*, IEEE Transactions on Geoscience and Remote
- 629 Sensing, 57 (2019), pp. 7119–7134.
- 630 [21] J. NUTTALL, *The convergence of Padé approximants of meromorphic functions*, J. Math. Anal.
- 631 Appl., 31 (1970), pp. 147–153, [https://doi.org/10.1016/0022-247X\(70\)90126-5](https://doi.org/10.1016/0022-247X(70)90126-5).
- 632 [22] H. NYQUIST, *Certain topics in telegraph transmission theory*, Trans. Am. Inst. Electr. Eng., 47
- 633 (1928), pp. 617–644, <https://doi.org/10.1109/T-AIEE.1928.5055024>.
- 634 [23] L. PEROTTI, T. REGIMBAU, D. VRINCEANU, AND D. BESSIS, *Identification of gravitational-wave*
- 635 *bursts in high noise using Padé filtering*, Physical Review D, 90 (2014), p. 124047.
- 636 [24] T. PETER, G. PLONKA, AND R. SCHABACK, *Prony's method for multivariate signals*, in PAMM
- 637 Proc. Appl. Math. Mech., vol. 15, 2015, pp. 664–666.
- 638 [25] C. POMMERENKE, *Padé approximants and convergence in capacity*, J. Math. Anal. Appl., 41
- 639 (1973), pp. 775–780, [https://doi.org/10.1016/0022-247X\(73\)90248-5](https://doi.org/10.1016/0022-247X(73)90248-5).
- 640 [26] D. POTTS AND M. TASCHE, *Parameter estimation for multivariate exponential sums*, Electronic
- 641 Transactions on Numerical Analysis, 40 (2013), pp. 204–224.
- 642 [27] A. QUINQUIS, E. RADOI, AND F.-C. TOTIR, *Some radar imagery results using superresolution*
- 643 *techniques*, IEEE Transactions on Antennas and Propagation, 52 (2004), pp. 1230–1244.
- 644 [28] S. ROUQUETTE AND M. NAJIM, *Estimation of frequencies and damping factors by two-*
- 645 *dimensional ESPRIT type methods*, IEEE Transactions on Signal Processing, 49 (2001),
- 646 pp. 237–245.
- 647 [29] R. ROY AND T. KAILATH, *ESPRIT-estimation of signal parameters via rotational invariance*
- 648 *techniques*, IEEE Trans. Acoust., Speech, Signal Process., 37 (1989), pp. 984–995, <https://doi.org/10.1109/29.32276>.
- 649 [30] S. SAHNOUN, K. USEVICH, AND P. COMON, *Multidimensional ESPRIT for Damped and Un-*
- 650 *damped Signals: Algorithm, Computations, and Perturbation Analysis*, IEEE Transactions
- 651 on Signal Processing, 65 (2017), pp. 5897–5910, [https://doi.org/10.1109/TSP.2017.](https://doi.org/10.1109/TSP.2017.2736512)
- 652 [2736512](https://doi.org/10.1109/TSP.2017.2736512).
- 653 [31] T. SAUER, *Prony's method in several variables: symbolic solutions by universal interpolation*,
- 654 Journal of Symbolic Computation, 84 (2018), pp. 95–112.
- 655 [32] C. E. SHANNON, *Communication in the presence of noise*, Proc. IRE, 37 (1949), pp. 10–21.
- 656 [33] L. WEISS AND R. McDONOUGH, *Prony's method, Z-transforms, and Padé approximation*,
- 657 SIAM Rev., 5 (1963), pp. 145–149.
- 658 [34] M. XING, R. WU, Y. LI, AND Z. BAO, *New ISAR imaging algorithm based on modified Wigner-*
- 659 *Ville distribution*, IET radar, sonar & navigation, 3 (2009), pp. 70–80.
- 660 [35] N. YILMAZER, S. ARI, AND T. K. SARKAR, *Multiple snapshot direct data domain approach and*
- 661 *ESPRIT method for direction of arrival estimation*, Digital Signal Processing, 18 (2008),
- 662 pp. 561–567, <https://doi.org/10.1016/j.dsp.2007.07.004>.
- 663 [36] L. ZHANG, Z. QIAO, M. XING, J. SHENG, R. GUO, AND Z. BAO, *High-resolution ISAR imaging*
- 664 *by exploiting sparse apertures*, IEEE Transactions on Antennas and Propagation, 60 (2012),
- 665 pp. 997–1008.
- 666 [37] J. ZHAO, M. ZHANG, X. WANG, Z. CAI, AND D. NIE, *Three-dimensional super resolution ISAR*
- 667 *imaging based on 2D unitary ESPRIT scattering centre extraction technique*, IET Radar,
- 668 Sonar & Navigation, 11 (2017), pp. 98–106.
- 669